Eng. Sci., 2022, **18**, 224–233

Engineered Science

DOI: https://dx.doi.org/10.30919/es8d529

Near-Field Radiative Heat Transfer via Coupling Graphene Plasmons with Different Phonon Polaritons in the Reststrahlen Bands

Ruiyi Liu,[1, 2] Lixin Ge,[3] Haiyan Yu,[2] Zheng Cui[1, 2,*] and Xiaohu Wu[2,*]

Abstract

Plasmon polaritons in graphene and phonon polaritons in polar materials or hyperbolic materials could enhance near-field radiative heat transfer (NFRHT). However, the detailed investigation of the coupling mechanism of graphene plasmons and different phonon polaritons in the Reststrahlen bands of the materials is insufficient. Here we systematically investigated the NFRHT between graphene-covered polar materials or hyperbolic materials in the Reststrahlen bands. Three types of bulk materials, *i.e.*, SiC, hBN, and α-MoO_3, are studied for comparisons. It is found that the coupling between graphene plasmons and surface phonon polaritons (SPhPs) in SiC could always suppress heat transfer. While the coupling between graphene plasmons and hyperbolic phonon polaritons (HPPs) in hBN could suppress or enhance the heat transfer, depending on the chemical potential of graphene. For graphene-covered α-MoO_3, it is found that the hyperbolic plasmon-phonon polaritons (HPPPs) always suppress the heat transfer, while the surface plasmon-phonon polaritons (SPPPs) could enhance or suppress the heat transfer, depending on the chemical potential of graphene and the frequencies. This work is helpful to deepen our understanding of the coupling mechanism between graphene plasmons and different kinds of phonon polaritons, and paves the way to manipulate the NFRHT of graphene-covered materials.

Keywords: Near-field radiative heat transfer; Graphene plasmons; Phonon polaritons; Hyperbolic materials; Photon tunneling.
Received: 04 July 2021; Revised: 11 September 2021; Accepted: 13 September 2021.
Article type: Research article.

1. Introduction

Near-field radiation heat transfer (NFRHT) has spurred many breakthroughs in the field of thermal radiation mainly due to the super-Planckian thermal radiation experiments.[1-3] The super-Planckian thermal radiation is attributed to the photon tunneling through evanescent waves, which are not taken into account in the far-field radiation.[4] The gigantic heat flux of NFRHT has potential applications in thermophotovoltaics,[5] thermal rectification,[6] noncontact refrigeration,[7] thermal transistors,[8] and so on.

The surface phonon polaritons (SPhPs) and surface plasmon polaritons (SPPs) excited in polar materials and metallic materials have been widely studied to facilitate photon tunneling.[9-11] In addition, hyperbolic materials can support the propagating waves of large wave vectors, and have attracted much attention.[12,13] In 2012, Biehs *et al*. proposed that the hyperbolic phonon polaritons (HPPs) excited in hyperbolic materials can greatly enhance the NFRHT.[14] Since this pioneering work, various hyperbolic materials have been explored to enhance photon tunneling.[15-21] Moreover, the super-Planckian thermal radiation in hyperbolic materials have been experimentally verified by Du *et al.*[22]

Being a two-dimensional material, graphene can generate plenty of resonance to promote photon tunneling.[23,24] In addition, graphene plasmons can be controlled by electrical gating, which renders graphene very promising for applications in NFRHT. By covering graphene sheets, the NFRHT between materials could be regulated. For instance, Liu *et al*. studied the NFRHT between graphene-covered silicon carbide (SiC) and observed the enhancement of the total heat flux.[25] Besides, Zhao and Zhang studied the NFRHT between graphene/hBN heterostructures, and also observed a significant increase in the total heat flux.[26] Although there are plenty of works considering the NFRHT in

[1] *Institute of Advanced Technology, Shandong University, Jinan 250061, China.*
[2] *Shandong Institute of Advanced Technology, Jinan 250100, China.*
[3] *School of Physics and Electronic Engineering, Xinyang Normal University, Xinyang 464000, China.*
**Email:* zhengc@sdu.edu.cn (Z. Cui),
xiaohu.wu@iat.cn (X. H. Wu)

graphene-covered systems,[27-33] the emphasis was solely on the enhancement of the total heat flux. The suppression of heat flux is also meaningful, such as the application of anti-heat (eliminating heat damage) and thermal modulators.[17,19,21] To understand the changing trend of heat flux and further utilize it, it is meaningful to study the influence of the polaritons coupling effect. However, the detailed investigation of the coupling mechanism of graphene plasmons and different phonon polaritons in the Reststrahlen bands of the materials is insufficient and its immense potential in the context of NFRHT remains largely untapped.

In this work, we comprehensively and comparatively investigate the NFRHT of different materials covered with graphene in the Reststrahlen bands. Specifically, materials from polar materials to hyperbolic materials are considered, including SiC, hBN, and α-MoO_3 biaxial crystals. Moreover, we analyze the energy transmission coefficient to reveal the coupling mechanism of graphene plasmons and different phonon polaritons. Our results show that in the Reststrahlen bands, the coupling between graphene plasmons and SPhPs in SiC could always suppress the heat flux. On the other hand, the coupling of graphene plasmons and HPPs in hBN could suppress or enhance the heat flux, depending on the chemical potential of the graphene. For graphene-covered α-MoO_3, the coupling between graphene plasmons and hyperbolic volume phonon polaritons (HVPPs) in α-MoO_3 always suppress the heat flux, while the coupling with hyperbolic surface phonon polaritons (HSPPs) could enhance or suppress the heat flux, depending not only on the chemical potentials but also on the frequencies. This work is helpful to deepen our understanding of the coupling between graphene plasmons and different phonon polaritons, and paves the way to manipulate the NFRHT of graphene-covered materials.

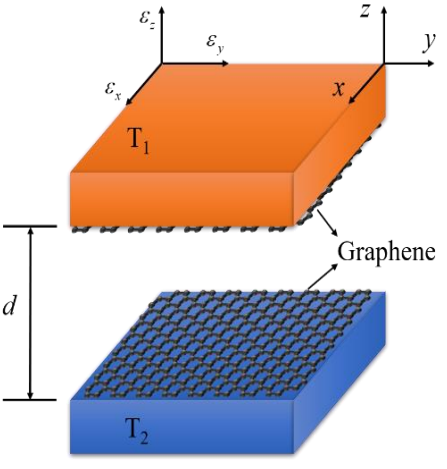

Fig. 1 Schematic of the NFRHT between bulk materials covered with graphene sheets. The temperatures of the emitter and receiver are T_1 and T_2, respectively.

2. Theory and methods

The configuration of NFRHT between graphene-covered materials (SiC, hBN, or α-MoO_3) is shown in Fig. 1. The distance between the emitter and receiver is d. The temperatures of the emitter and receiver are T_1 and T_2, respectively. In our calculations, T_1 and T_2 are set to 330 K and 300 K, respectively. The conductivity of graphene in the mid-infrared and far-infrared regions can be approximately written as[26]

$$\sigma_s = \frac{e^2\mu}{\pi\hbar^2}\frac{\tau}{1-j\omega\tau} \quad (1)$$

where e is the elementary charge, μ is the chemical potential, $\hbar$ is the reduced Planck constant, $\tau$is the relaxation time, and ω is the angular frequency. Here, $\tau = 10^{-13}s$ is chosen in our calculations. In the calculations, the graphene can be treated as a layer of thickness Δ = 0.3 nm with an effective permittivity $\varepsilon_{eff} = 1 + \frac{j\sigma_s}{\varepsilon_0\omega\Delta}$.

The dielectric constant of SiC can be obtained by the Lorentz model[11]

$$\varepsilon(\omega) = \varepsilon_\infty\left(\frac{\omega^2-\omega_{LO}^2+i\Gamma\omega}{\omega^2-\omega_{TO}^2+i\Gamma\omega}\right) \quad (2)$$

where ε_∞ = 6.7, ω_{LO} = 1.825×10^{14} rad/s, ω_{TO} = 1.494×10^{14} rad/s, and Γ = 8.966×10^{11} s^{-1}. As seen in Fig. 2(a), the real part of the dielectric constant of SiC is negative in the range from 1.50×10^{14} rad/s to 1.83×10^{14} rad/s, *i.e.*, the Reststrahlen band.

The hBN is a uniaxial hyperbolic crystal with out-plane anisotropy and in-plane isotropy in the infrared region. The dielectric constant of hBN can be described as diag($\varepsilon_\perp$,$\varepsilon_\perp$,$\varepsilon_\parallel$), where the optical axis lies in the z-direction. The in-plane and out-plane permittivity components are given as[26]

$$\varepsilon_m(\omega) = \varepsilon_{\infty,m}\left(1+\frac{\omega_{LO,m}^2-\omega_{TO,m}^2}{\omega_{TO,m}^2-\omega^2-i\omega\Gamma_m}\right) \quad (3)$$

where $m = \perp, \parallel$ means the component is vertical or parallel to the optic axis, $\omega_{TO,\perp}$ = 2.58×10^{14} rad/s, $\omega_{TO,\parallel}$ = 1.47×10^{14} rad/s, $\omega_{LO,\perp}$= 3.03×10^{14} rad/s, $\omega_{LO,\parallel}$= 1.56×10^{14} rad/s, $\varepsilon_{\infty,\perp}$ = 4.87, $\varepsilon_{\infty,\parallel}$ = 2.95, $\Gamma_\perp$ = 9.42×10^{11} s^{-1} and $\Gamma_\parallel$ = 7.54×10^{11} s^{-1}. The real parts of the relative permittivity components are shown in Fig. 2(b). As can be seen, there are two Reststrahlen bands for hBN. The first one is called the type I hyperbolic band with a frequency between 1.47×10^{14} rad/s and 1.56×10^{14} rad/s, in which $Re(\varepsilon_\perp) > 0$ and $Re(\varepsilon_\parallel) < 0$. The second one is called the type II hyperbolic band with a frequency between 2.58×10^{14} rad/s and 3.03×10^{14} rad/s, in which $Re(\varepsilon_\perp) < 0$ and $Re(\varepsilon_\parallel) > 0$.

For α-MoO_3 biaxial hyperbolic crystal, it possesses out-plane and in-plane anisotropy. The dielectric constant of α-MoO_3 can be described as diag(ε_x, ε_y, ε_z). The explicit expressions of ε_x, ε_y, and ε_z are the same as Eq. (3), where m = x, y, z, and the detailed parameters are $\omega_{LO,x}$ = 1.8322×10^{14} rad/s, $\omega_{LO,y}$ = 1.6041×10^{14} rad/s, $\omega_{LO,z}$ = 1.8925×10^{14} rad/s, $\omega_{TO,x}$ = 1.5457×10^{14} rad/s, $\omega_{TO,y}$ = 1.0273×10^{14} rad/s, $\omega_{TO,z}$ = 1.8058×10^{14} rad/s, $\varepsilon_{\infty,x}$ = 4, $\varepsilon_{\infty,y}$ = 5.2, $\varepsilon_{\infty,z}$ = 2.4, Γ_x = 7.5398×10^{11} s^{-1}, Γ_y = 7.5398×10^{11} s^{-1} and Γ_z = 3.7699×10^{11} s^{-1}.[19] As seen in Fig. 2(c), there are a negative signs for the real parts of ε_x, ε_y, or ε_z in a wide range from 1.03×10^{14} rad/s to 1.89×10^{14} rad/s, *i.e.*, the Reststrahlen band.

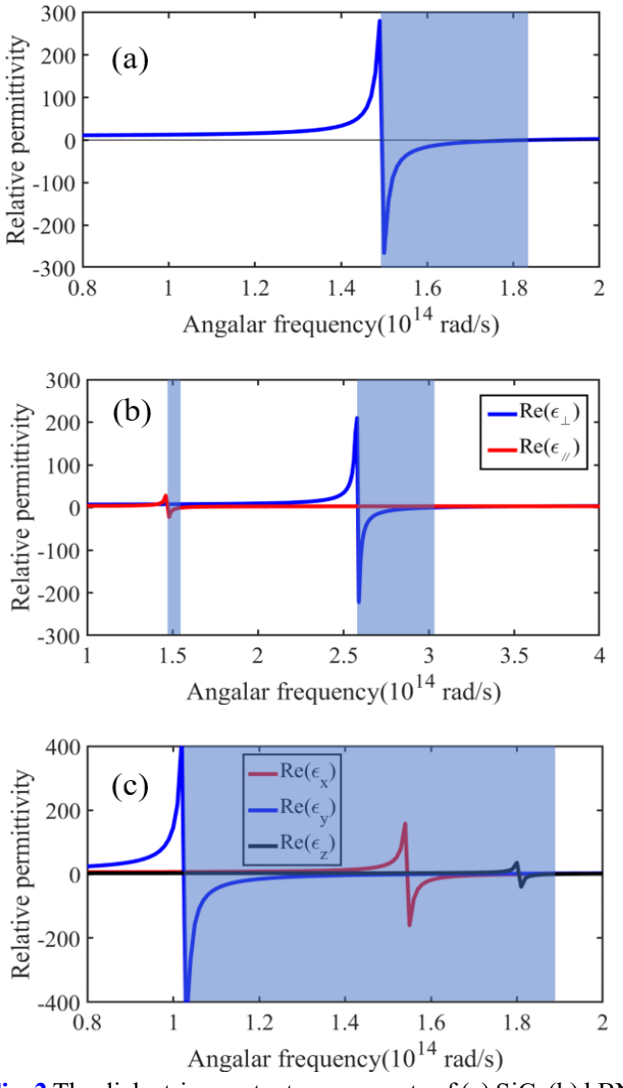

Fig. 2 The dielectric constant components of (a) SiC, (b) hBN, (c) α-MoO_3. The shaded areas indicate the Reststrahlen bands.

The NFRHT between medium 1 and medium 2 can be calculated by using the fluctuation-dissipation theorem and combining the dyadic Green's function, and the expression is

$$q = \frac{1}{4\pi^2}\int_0^\infty [\Theta(\omega,T_1)-\Theta(\omega,T_2)]d\omega \int_0^\infty \xi(\omega,\beta)\beta d\beta \quad (4)$$

where β is the parallel wavevector component, $\Theta(\omega,T)$ is the average energy of a Planck oscillator, $\xi(\omega,\beta)$ is called the energy transmission coefficient, whose explicit expression can be found in Ref.[26]. The $\xi(\omega,\beta)$ can be calculated by using the 4×4 transfer matrix method to solve the reflection and transmission coefficients.[18]

3. Results and discussion

3.1 NFRHT between two graphene-covered SiC slabs

Figure 3 shows the spectral heat flux of two graphene-covered bulk SiC, and the spectral heat flux of two bare bulk SiC is also calculated for comparison. In the frequency domain outside the Reststrahlen band of SiC, the spectral heat flux of two bare SiC slabs is almost zero, whereas the spectral heat flux of two graphene-covered SiC slabs can be greatly enhanced. In the Reststrahlen band, *i.e.*, 1.5×10^{14}~1.83×10^{14} rad/s, the spectral heat flux of bare bulk SiC can be significantly enhanced around 1.79×10^{14} rad/s. The resonant peak is attributed to the excitation of SPhPs, which has been observed in the published literature.[11] For graphene-covered bulk SiC, the heat flux is smaller than that of bare bulk SiC, regardless of the chemical potential. This phenomenon indicates that in the Reststrahlen band, the coupling between graphene plasmons and phonon polaritons in SiC can suppress the heat flux. Besides, the heat flux decreases with the increase of chemical potential.

To understand the changing trend of heat flux in the Reststrahlen band, Fig. 4 shows the energy transmission coefficients of different configurations. It is found that the SPhPs between two bare SiC slabs can be supported in a very large wavevector as given in Fig. 4(a), the energy carried by electromagnetic wave increases with the wavevector, and that is the reason for the heat flux peak in the Reststrahlen band. After adding graphene, the SPPs of graphene will couple with the SPhPs in SiC, producing hybrid polaritons called surface plasmon-phonon polaritons (SPPPs). As seen in Figs. 4(b-d), the wavevector for exciting SPPPs is reduced compared to that of SPhPs. Therefore, the heat flux of graphene-covered SiC decreases.

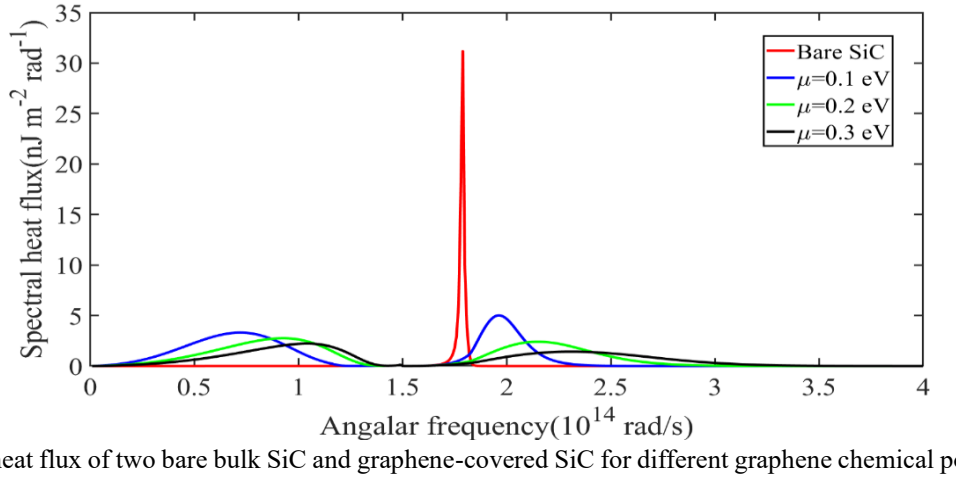

Fig. 3 The spectral heat flux of two bare bulk SiC and graphene-covered SiC for different graphene chemical potentials. The distance is d = 20 nm.

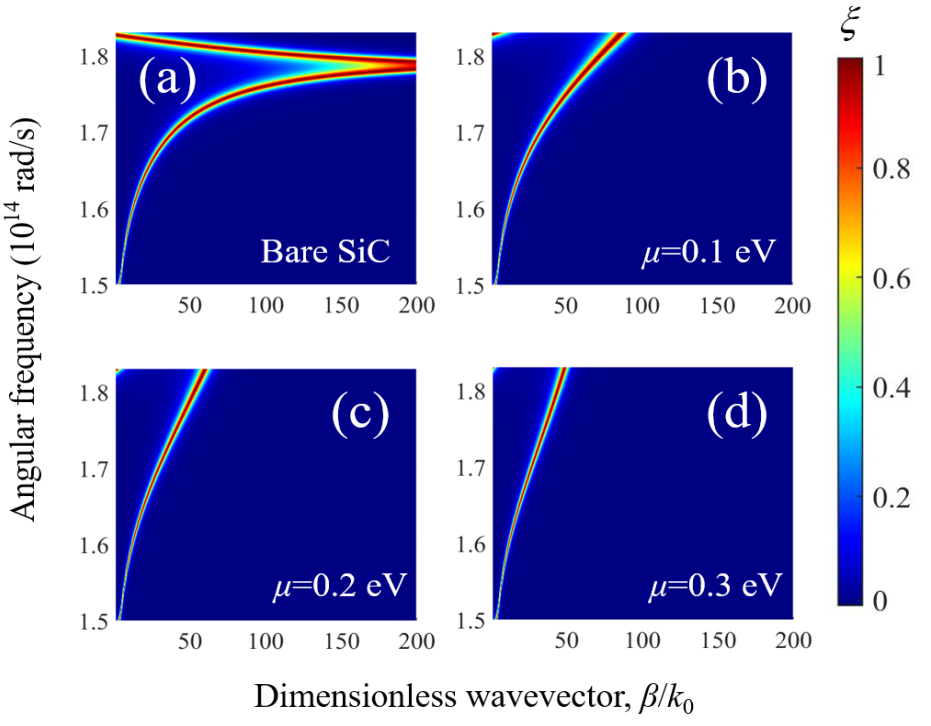

Fig. 4 Energy transmission coefficient for two bulk SiC with (or without) covering graphene sheets in the Reststrahlen band: (a) bare SiC, (b) 0.1 eV, (c) 0.2 eV, (d) 0.3 eV.

To present the underlying mechanism more clearly, the energy transmission coefficient varying with wavevector at 1.79×10^{14} rad/s (*i.e.* the peak frequency of the spectral heat flux of SiC) is shown in Fig. 5. Remarkably, the energy transmission coefficient for bare SiC keeps increasing with the wavevector until the wavevector reaches $200k_0$. When the wavevector is nearly $200k_0$, the energy transmission coefficient is close to 1. For graphene-covered SiC, the wavevector range of SPPPs decreases and does not exceed $100k_0$. As a result, the heat flux of graphene-covered SiC will be significantly decreased. Meanwhile, the spectrum of energy transmission coefficient becomes narrower and the peak is shifted to a smaller wavevector with the increasing of chemical potential, thus the heat flux decreases with the increase of chemical potential.

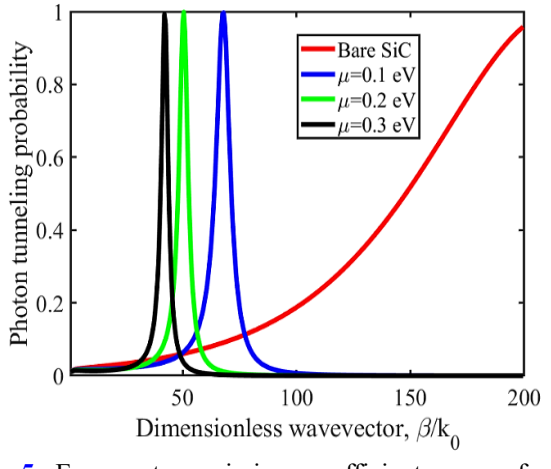

Fig. 5 Energy transmission coefficient as a function of wavevector for $\omega = 1.79\times10^{14}$ rad/s.

3.2 NFRHT between two graphene-covered hBN slabs

The hBN is a uniaxial crystal, which possesses hyperbolicity in the infrared region. Now we consider the NFRHT between two bulk hBN covered by graphene sheets. The spectral heat flux under different configurations is shown in Fig. 6. As can be seen, the spectral heat flux of bare bulk hBN can be greatly enhanced within the two Reststrahlen bands, whereas the magnitudes of the spectrum drop to nearly zero outside the Reststrahlen bands. After adding graphene, the spectra of the NFRHT show interesting features in type I hyperbolic band. As seen in Fig. 6(b), for chemical potential $\mu = 0.2$ eV and 0.3 eV, the spectral heat flux is suppressed compared to that of bare hBN, which is the same as that shown in Ref.[26]. As the chemical potential decreases to 0.1 eV, the heat flux of graphene-covered hBN can outperform that of bare hBN at the end of type I hyperbolic band. As seen in Fig. 6(c), in the type II hyperbolic band, after covering graphene for $\mu = 0.3$ eV, the heat flux does not change too much compared with that of bare hBN. Moreover, we find that the heat flux is suppressed when $\mu = 0.4$ eV, which is not shown here. By contrast, the heat flux is larger than that of bare hBN as the chemical potential μ is small, e.g., 0.1 eV and 0.2 eV. As a result, the spectra of NFRHT in two Reststrahlen bands show quite different trends with the chemical potential.

To understand the changing trend of heat flux in the type I hyperbolic band of different configurations, the corresponding energy transmission coefficients are shown in Fig. 7. For bare bulk hBN, there are HPPs excited in two Reststrahlen bands instead of SPhPs. After covering graphene, the coupling between SPPs of graphene and HPPs of hBN in the Reststrahlen bands can form hybrid polaritons called

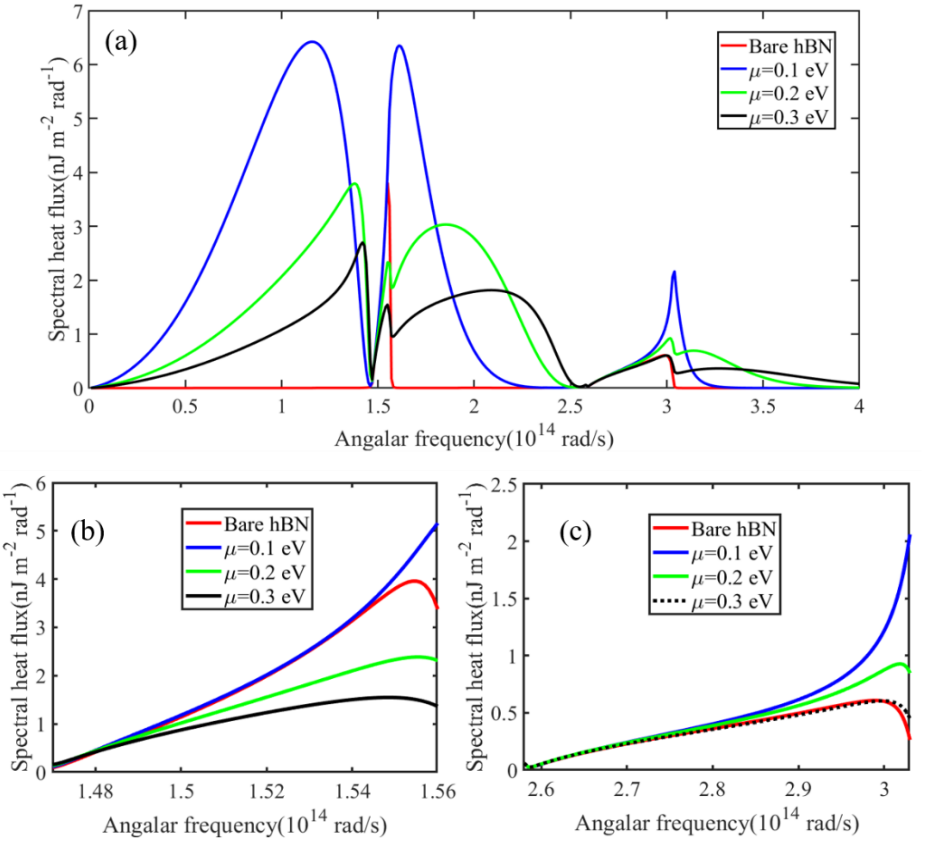

Fig. 6 The spectral heat flux of bulk hBN covered with (or without) graphene sheets in (a) 0~4×10^{14} rad/s, (b) type I hyperbolic band, (c) type II hyperbolic band. The distance is d = 20 nm.

hyperbolic plasmon-phonon polaritons (HPPPs).[26] Compared Fig. 7(b) with Fig. 7(a), one can see that when μ = 0.1 eV, the supported wavevector for HPPPs is enlarged near the upper end of the type I hyperbolic band, thus the heat flux of graphene-covered hBN can exceed that of bare hBN. Compared Figs. 7(c) and (d) with Fig. 7(b), the exciting wavevector for HPPPs decreases with increasing the chemical potential, thus the heat flux decreases.

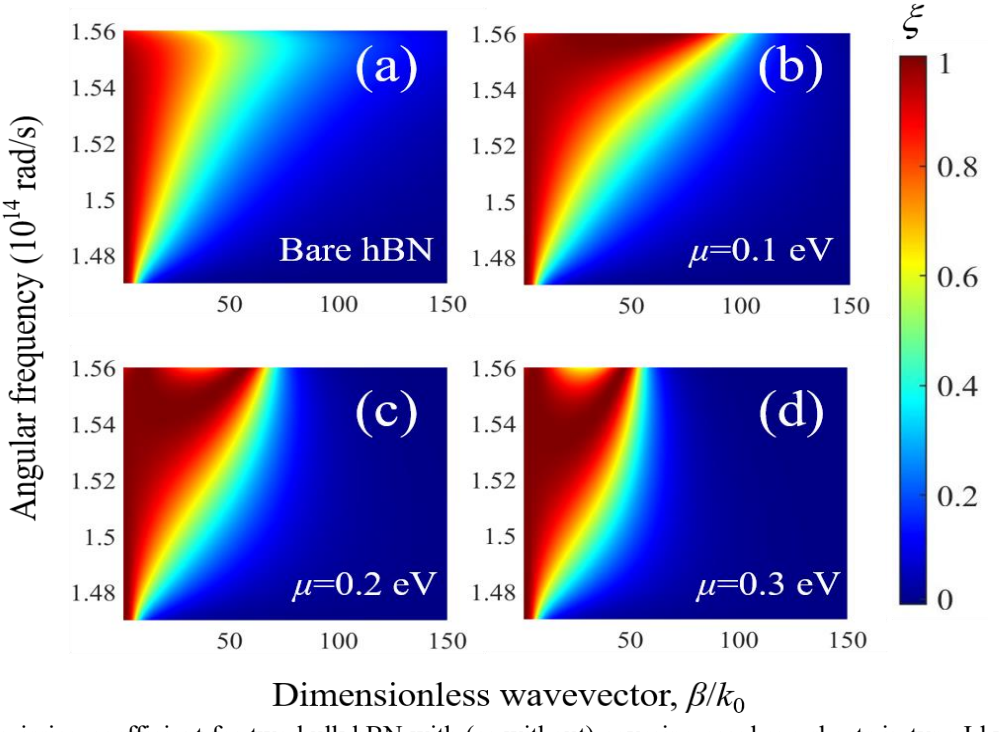

Fig. 7 Energy transmission coefficient for two bulk hBN with (or without) covering graphene sheets in type I hyperbolic band: (a) bare hBN, (b) 0.1 eV, (c) 0.2 eV, (d) 0.3 eV.

For a clearer analysis, we plotted the energy transmission coefficient varying with wavevector at the upper end of type I hyperbolic band (*i.e.* $\omega = 1.56\times10^{14}$ rad/s) in Fig. 8. Clearly, the energy transmission coefficient for $\mu = 0.1$ eV is greatly enhanced compared with the bare hBN case from 0 to about $120k_0$, thus the heat flux of graphene-covered hBN exceeds that of bare hBN. As μ increases to 0.2 eV and 0.3 eV, the wavevector range of energy transmission coefficient shrinks, and the coefficient drops to zero when the wavevector is larger than $100k_0$. However, the energy transmission coefficient of bare hBN is distributed in the whole wavevector range of $0\sim200k_0$. As a result, the heat flux decreases with the increase of chemical potential, for $\mu = 0.2$ eV and 0.3 eV, the heat flux is smaller than that of the bare case.

The energy transmission coefficients in the type II hyperbolic band of different configurations are shown in Fig. 9. For graphene-covered hBN slabs, the exciting HPPPs possess a larger wavevector in the upper half of type II hyperbolic band, compared to the case of bare hBN slabs. However, the wavevector for the exciting HPPPs decreases with the increase μ from 0.1 eV to 0.3 eV. For $\mu = 0.3$ eV, the wavevector for the HPPPs is nearly the same as that of HPPs in bare hBN, making the spectra almost overlap near 3.0×10^{14} rad/s.

The energy transmission coefficient at the upper end of the type II hyperbolic band (*i.e.* $\mu = 3.03\times10^{14}$ rad/s) is shown in Fig. 10. For $\mu = 0.1$ eV and 0.2 eV, the energy transmission coefficient is larger than that of bare hBN over a large wavevector range, resulting in the enhancement of heat flux. As the μ increases to 0.3 eV, the energy transmission coefficient is larger than that of bare hBN only when the wavevector $\beta < 70k_0$. However, the energy transmission coefficient decays and is slightly smaller than that of bare hBN when $\beta>70k_0$. As a result, the heat flux for $\mu = 0.3$ eV is almost the same as that of bare hBN.

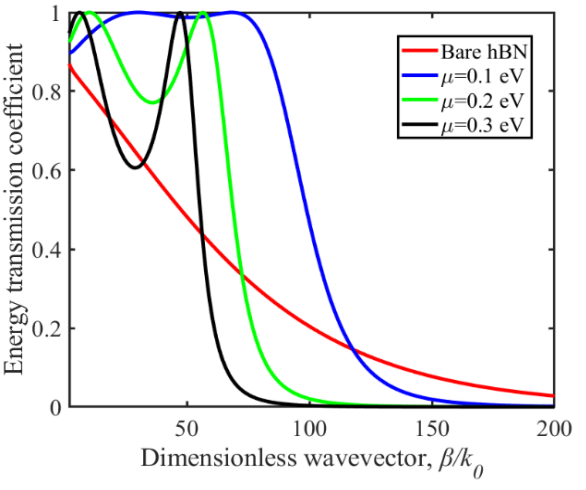

Fig. 8 Energy transmission coefficient as a function of wavevector for $\omega = 1.56\times10^{14}$ rad/s.

3.3 NFRHT between two graphene-covered α-MoO_3 slabs

The α-MoO_3 is a biaxial hyperbolic crystal, which excites the hyperbolic phonon polaritons in a wide frequency range. The spectral heat flux under different configurations is shown in Fig. 11. As expected, the heat flux of two bare bulk α-MoO_3 is enhanced in the Reststrahlen band from 1.03×10^{14} to 1.89×10^{14} rad/s and almost zero outside the Reststrahlen band,

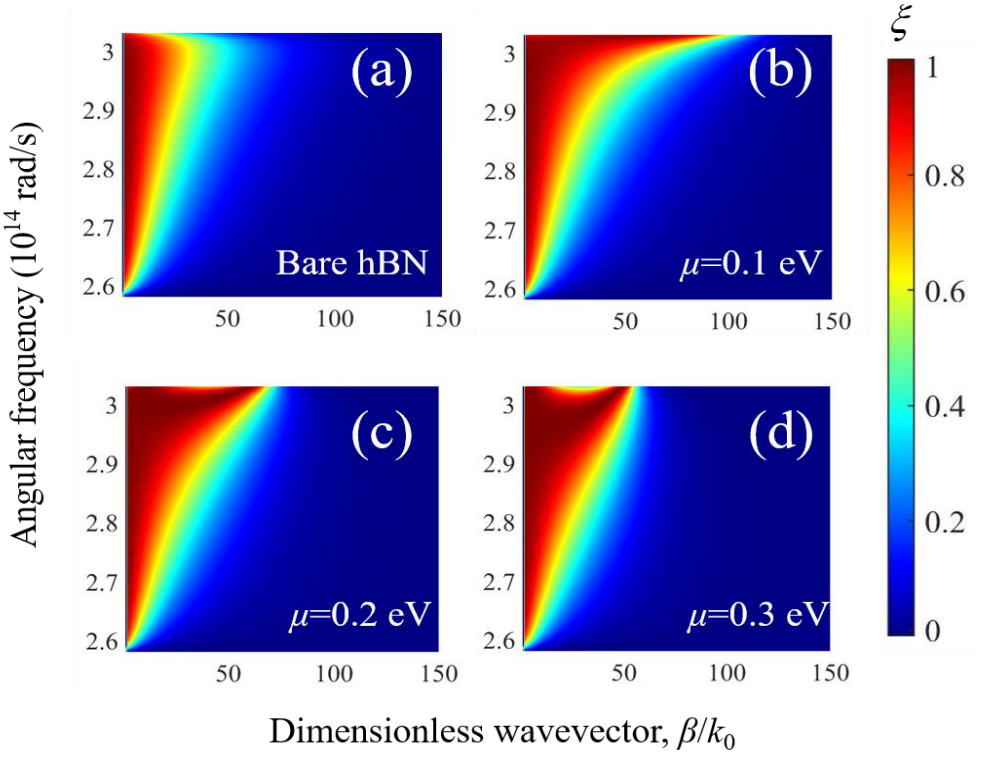

Fig. 9 Energy transmission coefficient for two bulk hBN with (or without) covering graphene sheets in type II hyperbolic band: (a) bare hBN, (b) 0.1 eV, (c) 0.2 eV, (d) 0.3 eV.

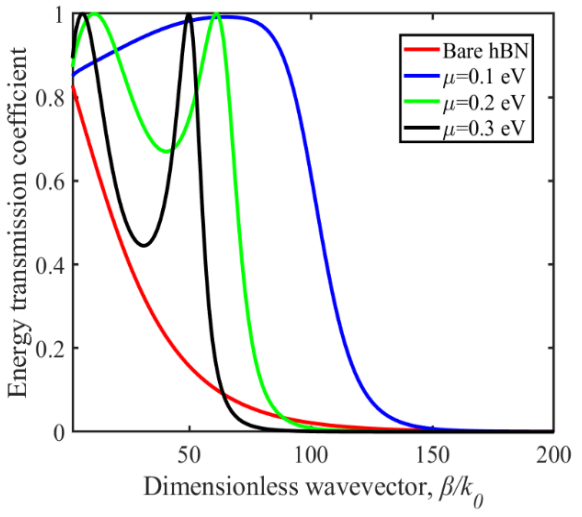

Fig. 10 Energy transmission coefficient as a function of wavevector for ω = 3.03×10^{14} rad/s.

which is the same as that shown in Ref.[19]. After adding graphene sheets, in most frequency domains of the Reststrahlen band, the heat flux of graphene-covered α-MoO_3 is significantly promoted when μ = 0.1 eV. As the μ increases to 0.2 eV and 0.3 eV, the heat flux can be suppressed or enhanced in different frequencies, and with the increase μ, the frequency domain of enhanced heat flux becomes smaller. Besides, no matter what the graphene chemical potential is, the heat flux of graphene-covered α-MoO_3 is always suppressed around the angular frequency of 1.82×10^{14} rad/s, which is the peak frequency of the heat flux for two bare bulk α-MoO_3. Therefore, the heat flux of graphene-covered α-MoO_3 can be suppressed or enhanced in the Reststrahlen band, depending not only on the chemical potentials but also on the frequencies.

Different from hBN, the HPPs excited in α-MoO_3 can be divided into two types: HSPPs and HVPPs.[19] In the Reststrahlen band, the coupling between SPPs in graphene and phonon polaritons in α-MoO_3 can produce two hybrid modes: SPPPs caused by the coupling between SPPs and HSPPs, and HPPPs due to the coupling between SPPs and HVPPs. The difference between SPPPs and HPPPs is that the later preserves the hyperbolic waveguide-mode features.[26] These hybrid modes make the NFRHT of graphene-covered α-MoO_3 more complex.

Similarly, we explain the trend in Fig. 11 by analyzing the energy transmission coefficient. Fig. 12 shows the energy transmission coefficients of different configurations at 1.35×10^{14} rad/s. At this frequency, for bare α-MoO_3, only HVPPs are excited on the upper and lower regions of wavevector space. The dispersion curves, *i.e.* the boundary curves of HVPPs are described as $k_y = \pm\sqrt{\frac{-\varepsilon_x}{\varepsilon_y}}k_x$.[19] The dielectric constants at this frequency are $\varepsilon_x = 10.8304 - 0.1227j$, $\varepsilon_y = -5.0862 - 0.1365j$ and $\varepsilon_z = 2.9351 - 0.0019j$, resulting in the boundary curves of $k_y = \pm 1.4592k_x$, denoted by the green dashed lines. As seen in Fig. 12(b), the two bright rings are the symmetric (low frequency) and asymmetric (high frequency) branches of the coupled SPPs in graphene, respectively.[26] After covering graphene with α-MoO_3, not only the HPPPs can be excited on the upper and lower regions, but also the SPPPs on the left and right regions. It can be seen that the boundary curves can clearly distinguish the contribution of SPPPs and HPPPs. In the excitation region of SPPPs, there are no polaritons excited for bare α-MoO_3, thus the excitation of SPPPs enhances the heat flux. For bare α-MoO_3, the excitation wavevector range of HVPPs exceeds $100k_0$, while that of HPPPs is less than $100k_0$, which means that HPPPs suppress the heat flux. For μ = 0.1 eV and 0.2 eV, although the energy transmission coefficient contributed by HPPPs is smaller than that of HVPPs, the energy transmission coefficient for SPPPs is distributed in a wider wavevector range, thus the heat flux of grapheme-covered α-MoO_3 can be greatly enhanced compared with the case of bare α-MoO_3 due to the excitation of SPPPs. As the μ increases to 0.3 eV, both the excitations of SPPPs and HPPPs shrink to smaller wavevector, and the wavevectors of SPPPs and HPPPs do not exceed $100k_0$, while the HVPPs of bare α-

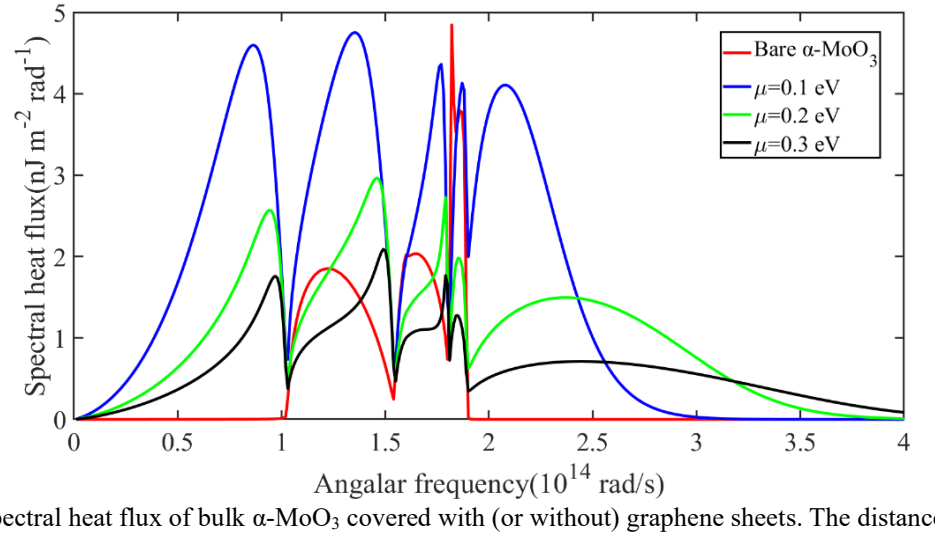

Fig. 11 The spectral heat flux of bulk α-MoO_3 covered with (or without) graphene sheets. The distance is d = 20 nm.

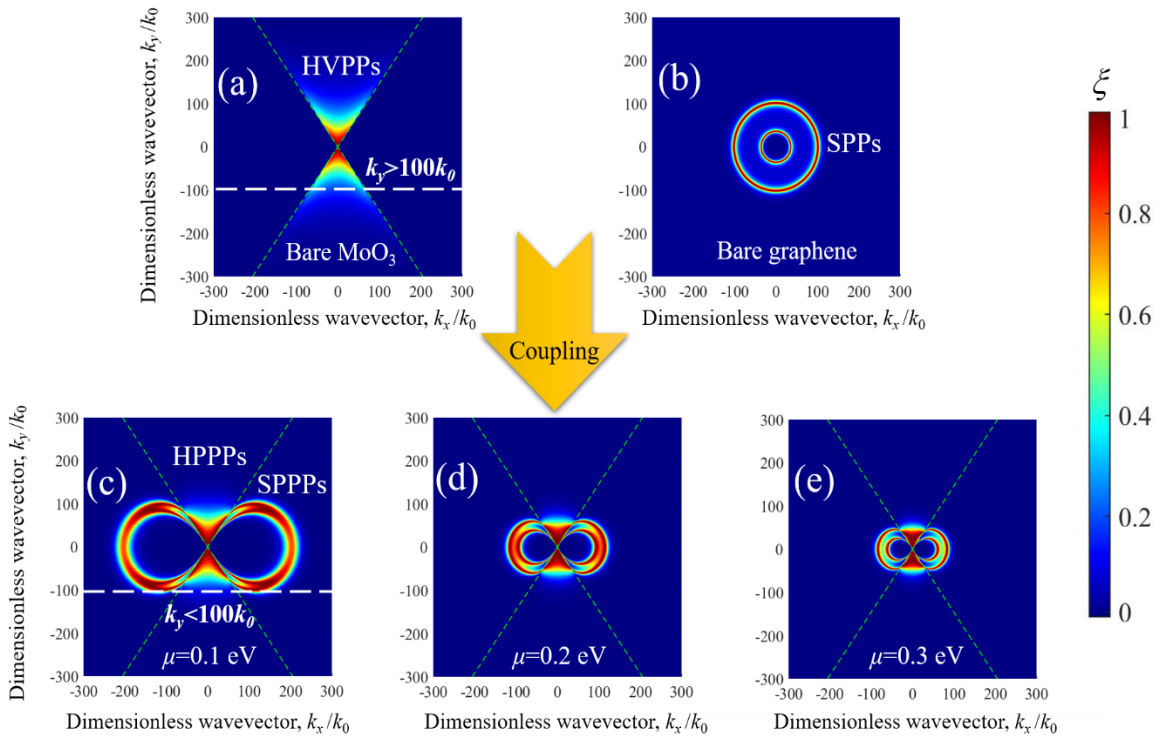

Fig. 12 Energy transmission coefficient as a function of wavevector components at 1.35×10^{14} rad/s for: (a) bare α-MoO_3, (b) bare graphene with ω = 0.1 eV, graphene-covered α-MoO_3 with chemical potential of (c)0.1 eV, (d) 0.2 eV, and (e) 0.3 eV.

MoO_3 can still be excited at around 150k_0, thus the heat flux after covering graphene is suppressed. Therefore, the graphene chemical potential plays an important role in the coupling of graphene plasmons and phonon polaritons in α-MoO_3, resulting in suppressing or enhancing the heat flux.

In Fig. 13, we consider the energy transmission coefficients of different configurations at the peak frequency of the heat flux for two bare bulk α-MoO_3 (*i.e.* ω = 1.82×10^{14} rad/s). At this frequency, the dielectric constants are $\varepsilon_x = -0.1917 - 0.0623j$, $\varepsilon_y = 1.7033 - 0.0213j$ and $\varepsilon_z = -12.2745 - 1.9539j$, resulting in the boundary curves of $k_y = \pm 0.3355 k_x$ (the green dashed lines). For bare α-MoO_3, not only HVPPs can be excited on the upper and lower regions of wavevector space, but also HSPPs on the left and right regions, and can be clearly distinguished by the boundary curves. It can be seen that HVPPs and HSPPs, especially HSPPs, can be

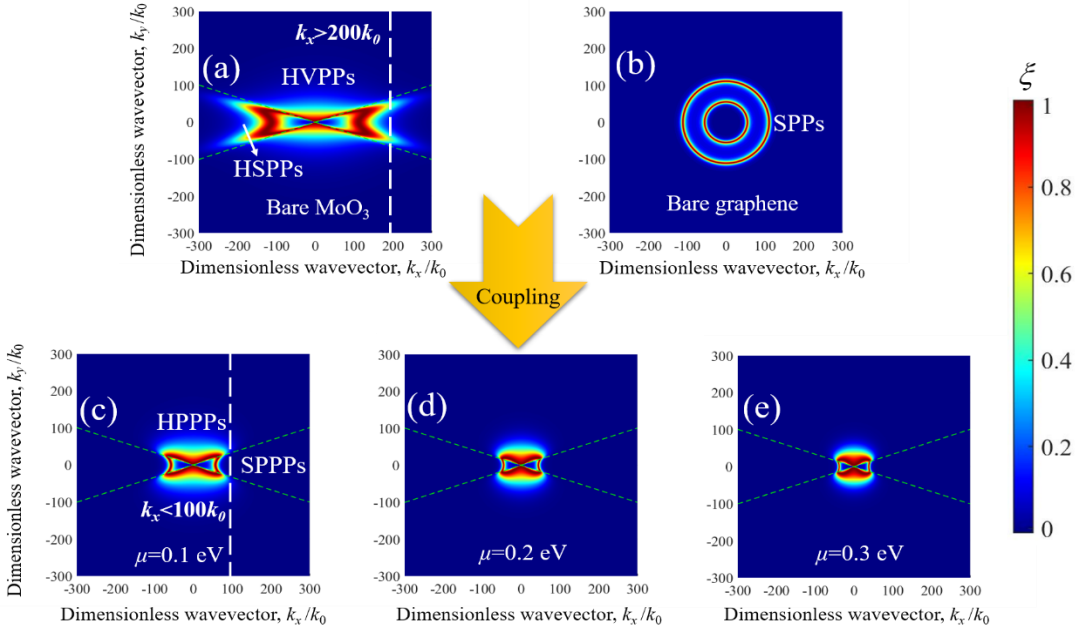

Fig. 13 Energy transmission coefficient as a function of wavevector components at 1.82×10^{14} rad/s for: (a) bare α-MoO_3, (b) bare graphene with μ = 0.1 eV, graphene-covered α-MoO_3 with chemical potential of (c)0.1 eV, (d) 0.2 eV, and (e) 0.3 eV.

excited at large wavevector, leading to the peak of heat flux for bare α-MoO_3 at this frequency in Fig. 11. As seen in Fig. 13(b), the excitation wavevector range of SPPs in graphene decreases compared with Fig. 12(b). As can be seen, the k_y wavevector of HPPPs is almost the same as that of HVPPs, whereas the k_x wavevector is smaller than that of HVPPs, thus the HPPPs suppress the heat flux. For the SPPPs, the excitation wavevector is less than $100k_0$, while that of HSPPs is more than $200k_0$, thus the SPPPs also suppress the heat flux. Therefore, both two hybrid modes suppress the heat flux, so the heat flux after covering graphene is greatly suppressed. Moreover, with the increasing of μ from 0.1 eV to 0.3 eV, the excitation regions of SPPPs and HPPPs shrink to the origin. As a result, the heat flux will decrease with the increase of chemical potential.

4. Conclusions

In summary, we have investigated the NFRHT between graphene-covered polar materials and hyperbolic materials in Reststrahlen bands and compared the results to configurations of bare bulk materials, respectively. For SiC, the comparison shows that the heat flux via coupling between graphene plasmons and SPhPs in the Reststrahlen band is always suppressed. For hBN uniaxial crystal, the coupling between graphene plasmons and HPPs in hBN could suppress or enhance the heat flux, depending on the chemical potential of graphene. For α-MoO_3 biaxial crystal, there are HVPPs and HSPPs excited in the Reststrahlen band, the coupling between them and graphene plasmons can form two hybrid modes such as HPPPs and SPPPs. It is found that the HPPPs always suppress the heat transfer, while the SPPPs could enhance or suppress the heat transfer. The coupling between graphene plasmons and phonon polaritons in α-MoO_3 could suppress or enhance the heat flux in the Reststrahlen band, depending on the chemical potential of graphene and the frequencies. This work is helpful to deepen our understanding of the coupling mechanism between graphene plasmons and different kinds of phonon polaritons, and paves the way for controlling the NFRHT of graphene-covered materials.

Conflict of interest

There are no conflicts to declare.

Supporting information

Not applicable.

References

[1] L. Hu, A. Narayanaswamy, X. Chen, G. Chen, *Applied Physics Letters*, 2008, **92**, 133106, doi: 10.1063/1.2905286.

[2] M. Lim, J. Song, S. S. Lee, B. J. Lee, *Nature Communications*, 2018, **9**, 4302, doi: 10.1038/s41467-018-06795-w.

[3] P. Sabbaghi, L. Long, X. Ying, L. Lambert, S. Taylor, C. Messner, L. Wang, *Journal of Applied Physics*, 2020, **128**, 025305, doi: 10.1063/5.0008259.

[4] S. Basu, Z. M. Zhang, C. J. Fu, *International Journal of Energy Research*, 2009, **33**, 1203-1232, doi: 10.1002/er.1607.

[5] R. Messina, P. Ben-Abdallah, *Scientific Reports*, 2013, **3**, 1383, doi: 10.1038/srep01383.

[6] L. Zhu, C. R. Otey, S. Fan, *Physical Review B*, 2013, **88**, 184301, doi: 10.1103/physrevb.88.184301.

[7] K. Chen, P. Santhanam, S. Fan, *Physical Review Applied*, 2016, **6**, 024014, doi: 10.1103/physrevapplied.6.024014.

[8] P. Abdallah, S. Biehs, *Physical Review Letters*, 2014, **112**, 044301, doi: 10.1103/physrevlett.112.044301.

[9] Y. Zhang, H.-L. Yi, H.-P. Tan, *ACS Photonics*, 2018, **5**, 3739-3747, doi: 10.1021/acsphotonics.8b00776.

[10] B. Song, Y. Ganjeh, S. Sadat, D. Thompson, A. Fiorino, V. Fernández-Hurtado, J. Feist, F. J. Garcia-Vidal, J. C. Cuevas, P. Reddy, E. Meyhofer, *Nature Nanotechnology*, 2015, **10**, 253-258, doi: 10.1038/nnano.2015.6.

[11] M. Francoeur, M. P. Mengüç, R. Vaillon, *Journal of Physics D: Applied Physics*, 2010, **43**, 075501, doi: 10.1088/0022-3727/43/7/075501.

[12] X. Wu, C. A. McEleney, M. González-Jiménez, R. Macêdo, *Optica*, 2019, **6**, 1478, doi: 10.1364/optica.6.001478.

[13] X. H. Wu, C. J. Fu, Z. M. Zhang, *International Journal of Heat and Mass Transfer*, 2019, **135**, 1207-1217, doi: 10.1016/j.ijheatmasstransfer.2019.02.066.

[14] S.-A. Biehs, M. Tschikin, P. Ben-Abdallah, *Physical Review Letters*, 2012, **109**, 104301, doi: 10.1103/physrevlett.109.104301.

[15] Y. Guo, C. L. Cortes, S. Molesky, Z. Jacob, *Applied Physics Letters*, 2012, **101**, 131106, doi: 10.1063/1.4754616.

[16] S. A. Biehs, M. Tschikin, R. Messina, P. Ben-Abdallah, *Applied Physics Letters*, 2013, **102**, 131106, doi: 10.1063/1.4800233.

[17] X. L. Liu, J. D. Shen, Y. M. Xuan, *Journal of Quantitative Spectroscopy and Radiative Transfer*, 2017, 200, **100**, doi: 10.1016/j.jqsrt.2017.06.010,

[18] X. H. Wu, C. J. Fu, Z. M. Zhang, *Journal of Photonics for Energy*, 2018, **9**, 032702, doi: 10.1117/1.JPE.9.032702.

[19] X. H. Wu, C. J. Fu, Z. M. Zhang, *Journal of Heat Transfer*, 2020, **142**, 072802, doi: 10.1115/1.4046968.

[20] X. H. Wu, C. J. Fu, *Journal of Quantitative Spectroscopy and Radiative Transfer*, 2021, **258**, 107337, doi: 10.1016/j.jqsrt.2020.107337.

[21] X. H. Wu, C. J. Fu, *International Journal of Heat and Mass Transfer*, 2021, **168**, 120908, doi: 10.1016/j.ijheatmasstransfer.2021.120908.

[22] W. Du, J. Yang, S. Zhang, N. Iqbal, Y. Dang, J.-B. Xu, Y. Ma, *Nano Energy*, 2020, **78**, 105264, doi: 10.1016/j.nanoen.2020.105264.

[23] F. Xia, H. Wang, D. Xiao, M. Dubey, A. Ramasubramaniam, *Nature Photonics*, 2014, **8**, 899-907, doi: 10.1038/nphoton.2014.271.

[24] J. Yang, W. Du, Y. Su, Y. Fu, S. Gong, S. He, Y. Ma, *Nature Communications*, 2018, **9**, 4033, doi: 10.1038/s41467-018-06163-8.

[25] D. Y. Xu, J. M. Zhao, L. H. Liu, *Journal of Engineering Thermophysics*, 2020, **41**, 715-721.

[26] B. Zhao, Z. M. Zhang, *Journal of Heat Transfer*, 2017, **139**,

022701, doi: 10.1115/1.4034793.
[27] A. Wang, Z. H. Zheng, Y. M. Xuan, *Journal of Quantitative Spectroscopy and Radiative*, 2016, **180**, 117-125, doi: 10.1016/j.jqsrt.2016.04.018.
[28] M. Lim, S. S. Lee, B. J. Lee, *Optics Express*, 2013, **21**, 22173, doi: 10.1364/oe.21.022173.
[29] R. Messina, P. Ben-Abdallah, B. Guizal, M. Antezza, *Physical Review B*, 2017, **96**, 045402, doi: 10.1103/physrevb.96.045402.
[30] X. Wu, R. Liu, *ES Energy & Environment*, 2020, **10**, 66-72.doi: 10.30919/esee8c939.
[31] B. Zhao, B. Guizal, Z. M. Zhang, S. Fan, M. Antezza, *Physical Review B*, 2017, **95**, 245437, doi: 10.1103/physrevb.95.245437.
[32] K. Shi, F. Bao, S. He, *ACS Photonics*, 2017, **4**, 971-978, doi: 10.1021/acsphotonics.7b00037.
[33] Y. Zhang, C.-H. Wang, H.-L. Yi, H.-P. Tan, *Journal of Quantitative Spectroscopy and Radiative Transfer,* 2018, **221**, 138-146, doi: 10.1016/j.jqsrt.2018.09.029.

Author Information

Xiaohu Wu *received his B.S. degree in engineering mechanics from China University of Mining and Technology (Beijing) and Ph. D. degree from Peking University under the guidance of Prof. Ceji Fu. He was a visiting student at Georgia Institute of Technology from Sept. 2017 to Sept. 2018 under the guidance of Prof. Zhuomin Zhang. Currently, Dr. Wu is an associate researcher at Shandong Institute of Advanced Technology. Dr. Wu's main research interest is on thermal radiative properties of anisotropic materials and applications. He has published about 50 peer-reviewed journal papers and given three conference presentations. His Ph.D. thesis was published by Springer Nature and was recognized as outstanding doctoral research. Dr. Wu is the winner (along with his advisors) of the 2019 Hartnett-Irvine Award by the International Centre for Heat and Mass Transfer. In addition, his work about hyperbolic materials was selected as "Optics in 2020" by Optics & Photonics News. Besides, two of his papers are selected as cover papers. He is one of the early-career editorial board members of ES Energy & Environment.*